Draft version December 4, 2025
Typeset using LaTeX **twocolumn** style in AASTeX7.0.1

(Re)solving the complex multi-scale morphology and V-shaped SED of a newly discovered strongly-lensed Little Red Dot in Abell 383

Josephine F.W. Baggen [1], Pieter van Dokkum [1], Ivo Labbé [2], and Gabriel Brammer [3]

[1] *Department of Astronomy, Yale University, New Haven, CT 06511, USA*
[2] *Centre for Astrophysics and Supercomputing, Swinburne University of Technology, Melbourne, VIC 3122, Australia*
[3] *Cosmic Dawn Center (DAWN), Niels Bohr Institute, University of Copenhagen, Jagtvej 128, København N, DK-2200, Denmark*

ABSTRACT

We present a luminous Little Red Dot (LRD) at $z = 6.027$, doubly imaged by the galaxy cluster Abell 383 and observed with JWST/NIRCam. The source shows the characteristic "V-shaped" SED and pronounced Balmer break that define the LRD population. Owing to its large magnifications, $\mu \sim 11$ for image S1 and $\mu \sim 7$ for S2, the system is exceptionally bright and highly stretched, providing a rare, spatially resolved view of an LRD. The images reveal a complex morphology with a compact red dot, a spatially offset blue dot, and faint emission bridging and surrounding the two. After correcting for lensing, we find that both dots are extremely small but resolved, with rest-frame UV sizes of ~ 20 pc (red) and ~ 60 pc (blue). These compact dots are embedded in a more extended, line-dominated cloud traced most clearly in F356W ([OIII]+Hβ), which reaches scales of order $\sim$1 kpc. SED decomposition shows that the blue component has a flat UV continuum consistent with a young stellar population, whereas the red component has a steep red SED that can be interpreted as either an evolved stellar population with high stellar mass ($\log M_\star/M_\odot > 10$) or a reddened AGN. If this object is representative of the LRD population, our results imply that the V-shaped SEDs of LRDs do not arise from individual compact sources but instead from the superposition of two physically distinct components. Separated by only ~ 300 pc in the source plane, these components would blend into a single compact source in unlensed observations with the canonical LRD colors. This system therefore provides a rare opportunity to resolve the internal structure of an LRD and to gain direct insight into the physical nature of this population.

Keywords: cosmology: observations — galaxies: evolution — galaxies: formation

1. INTRODUCTION

The James Webb Space Telescope (JWST) is transforming our view of the earliest phases of galaxy and black hole formation. Among its most surprising discoveries is a population of compact, red sources seen across many surveys (e.g., D. D. Kocevski et al. 2023; I. Labbé et al. 2023; Y. Harikane et al. 2023; R. Maiolino et al. 2024; J. Matthee et al. 2024; V. Kokorev et al. 2024; H. B. Akins et al. 2024), now colloquially termed "Little Red Dots" (LRDs).

The properties of LRDs are unusual, making them difficult to interpret within standard models. In the optical, they show extremely red continua (L. J. Furtak et al. 2024), compact morphologies (e.g., J. F. W. Baggen et al. 2023, 2024; H. B. Akins et al. 2023), broad Balmer lines (J. Matthee et al. 2024; J. E. Greene et al. 2024; D. D. Kocevski et al. 2023; Y. Harikane et al. 2023; R. Maiolino et al. 2024), and frequent Balmer breaks (B. Wang et al. 2024; A. de Graaff et al. 2025; R. P. Naidu et al. 2025; I. Labbe et al. 2024). At the same time, LRDs exhibit blue colors in the rest-frame UV (e.g., D. D. Kocevski et al. 2024, and references therein). Short-wavelength JWST imaging further reveals that this UV emission is often irregular, and spatially offset from the red emission (P. Rinaldi et al. 2024; J. F. W. Baggen et al. 2024; C.-H. Chen et al. 2025). When combined, the integrated light from the rest-UV to rest-optical forms a distinctive "V-shaped" spectral energy distribution (SED), with the inflection point occurring consistently at the Balmer limit (D. J. Setton et al. 2024; D. D. Kocevski et al. 2024; R. E. Hviding et al. 2025).

Email: josephine.baggen@yale.edu

A leading model to explain these features is that they are produced by AGNs (J. E. Greene et al. 2024; J. Matthee et al. 2024; D. D. Kocevski et al. 2024). However, LRDs lack nearly all canonical signatures of accretion: they are X-ray faint (T. T. Ananna et al. 2024), radio-quiet (A. J. Gloudemans et al. 2025), lack hot dust emission (P. G. Pérez-González et al. 2024; C. C. Williams et al. 2024; D. J. Setton et al. 2025), and lack hard ionizing photons (B. Wang et al. 2025), show little or no variability (e.g. C. J. Burke et al. 2025), and their SEDs favor stellar over AGN templates (P. G. Pérez-González et al. 2024; M. Carranza-Escudero et al. 2025). This has motivated more exotic scenarios in which the black hole is hidden within dense, optically thick gas (K. Inayoshi & R. Maiolino 2025; X. Ji et al. 2025; F. D'Eugenio et al. 2025a; I. Juodžbalis et al. 2024), producing an A-type star-like spectrum with a strong Balmer break. Such "black-hole–star systems" (BH*) (R. P. Naidu et al. 2025; A. de Graaff et al. 2025) may lack a stellar host entirely (I. Juodžbalis et al. 2025). A related possibility is that some LRDs are late-stage quasi-stars (M. C. Begelman et al. 2006; M. C. Begelman & J. Dexter 2025); synthetic spectra from these models show promising agreement with observations (A. D. Santarelli et al. 2025). In all these scenarios the UV emission is thought to arise from regions close to the black hole, either in the form of scattered AGN light (G. C. K. Leung et al. 2025; J. E. Greene et al. 2024; L. J. Furtak et al. 2023) or nebular continuum from low-density gas (C.-H. Chen et al. 2025).

An alternative idea is that the light in both the rest-frame UV and optical comes from stars. In the optical, this would imply both evolved stellar populations and significant dust absorption (e.g., I. Labbé et al. 2023; B. Wang et al. 2024; H. B. Akins et al. 2023; G. Barro et al. 2024), yielding extreme stellar masses (I. Labbé et al. 2023; B. Wang et al. 2024). The high masses combined with the small sizes of LRDs lead to extremely high inferred stellar densities, and the observed broad Balmer lines are explained by virial motions alone (J. F. W. Baggen et al. 2024). In this scenario the UV emission simply traces regions of relatively unobscured star formation, consistent with the absence of MgII λ2800 (H. B. Akins et al. 2025) expected for the AGN scattering scenario, spatially resolved narrow lines and UV continua (M. Killi et al. 2024), and the extended complex, sometimes offset UV morphologies (M. Killi et al. 2024; P. Rinaldi et al. 2024; J. F. W. Baggen et al. 2024; C.-H. Chen et al. 2025).

Much of the effort to discriminate between these scenarios has been focused on the interpretation of the spectra and SEDs of LRDs. The internal structure of LRDs provides – in principle – an important additional constraint. In the "naked" black hole scenarios all emission is centered on the black hole and extremely compact; as an example, the "quasi-star" picture should have a size of only up to a few thousand AU (0.02 pc) (M. C. Begelman & J. Dexter 2025). By contrast, in stellar-dominated models the galaxies should show a spatially-resolved morphology at sufficiently high spatial resolution, with the size of the dominant mass component given by $r_e \sim M/\sigma^2$.

The only practical way to obtain the necessary resolution is through strong gravitational lensing. To date, only a single LRD has been studied in such detail, a triply lensed, intrinsically faint system in Abell 2744 (A2744-QSO1) magnified by a factor of ~ 7 (L. J. Furtak et al. 2023, 2024; J. E. Greene et al. 2024). This source has been observed with IFU spectroscopy at high spatial resolution (X. Ji et al. 2025; F. D'Eugenio et al. 2025b), and supports a minimal host-galaxy contribution observed emission (I. Juodžbalis et al. 2025). Here we present a second strongly-lensed LRD that is more than an order of magnitude brighter than A2744-QSO1.

Throughout this paper, we adopt the flat Planck18 CDM cosmology (with BAO constraints, Table 2 in Planck Collaboration VI 2020), and report all magnitudes in the AB system.

2. A STRONGLY-LENSED LRD BEHIND ABELL 383

2.1. *Observations and Identification*

The source was identified in NIRCAM imaging of the cluster Abell 383. The primary data used in this work are JWST/NIRCam observations from the VENUS program (Program ID: GO 6882; PI: S. Fujimoto), supplemented by HST/ACS and HST/WFC3 imaging from the CLASH survey (M. Postman et al. 2012). All data were reduced using the `grizli` pipeline (G. Brammer et al. 2022). The final mosaics used in this work contain 17 filters: HST/ACS (F435W, F606W, F775W, F814W), HST/WFC3 (F110W, F125W, F140W, F160W), and JWST/NIRCam (F090W, F115W, F150W, F200W, F210M, F277W, F356W, F410M, F444W). The NIRCam mosaics have pixel scales of 0.″02 and 0.″04 for the short-wavelength (SW; $\lambda < 2.4\,\mu$m) and long-wavelength (LW; $\lambda > 2.4\,\mu$m) channels, respectively. All HST mosaics are drizzled to 0.″04/pixel.

We show a composite color image of Abell 383 made from the JWST/NIRCam mosaics in Figure 1. Two compact red objects (here named S1 and S2) are apparent in the cluster field. These sources were first identified as lensed high-redshift galaxies in the CLASH survey, with $z_{\rm spec} = 6.027$ and extreme magnifications derived

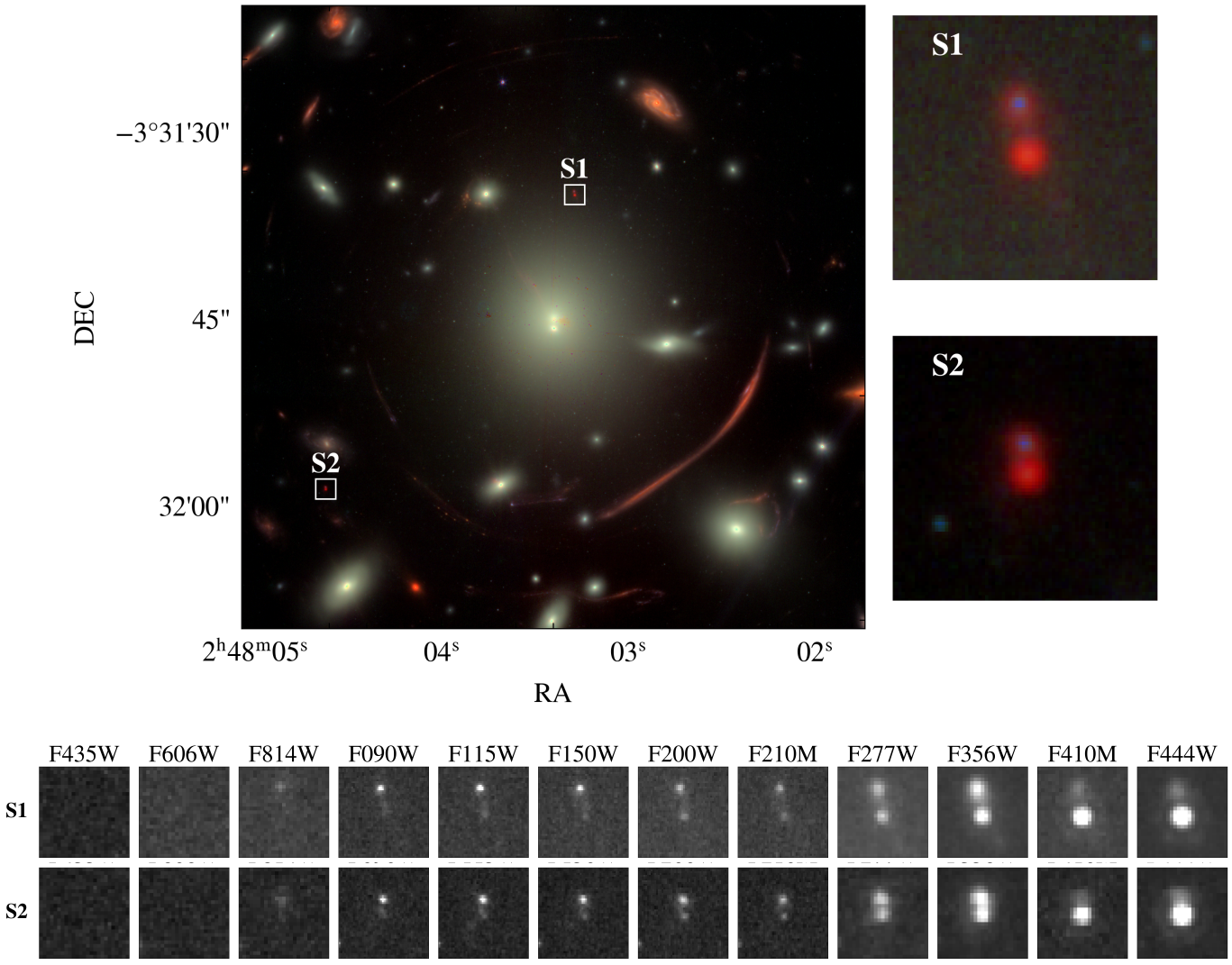

Figure 1. Top: RGB composite image of Abell 383, constructed using F090W + F115W + F150W for blue, F200W + F210M for green, and F277W + F356W + F444W for red. Inset cutouts show the doubly-lensed system (S1 and S2) and are $1.6'' \times 1.6''$. Bottom: Multi-band cutouts ($1.0'' \times 1.0''$) for images S1 and S2 across HST and JWST filters.

from best-fitting lensing models of $\mu_1 = 11.4 \pm 1.9$ and $\mu_2 = 7.3 \pm 1.2$ (J. Richard et al. 2011; D. P. Stark et al. 2015).

2.2. *Total Photometry and Spectral Energy Distribution*

We performed PSF-matched aperture photometry on $10'' \times 10''$ cutouts centered on both S1 and S2 using all available HST and JWST imaging. To account for the varying point spread functions (PSFs) across instruments and wavelengths, all images were convolved to match the F444W PSF using empirical PSF models and matching kernels from J. R. Weaver et al. (2024). Background subtraction was applied to the PSF-matched images using a sigma-clipped 2D median filter computed in 25×25 pixel boxes, followed by an additional 5×5 pixel median smoothing to generate a background model. Photometry was then performed with `photutils` (L. Bradley et al. 2025) on the background-subtracted images, using circular apertures with a radius of $0.5''$. Flux uncertainties were estimated empirically by measuring the rms of 1000 empty apertures of the same radius placed in source-free background regions of these images. Aperture corrections, derived from the PSF-matched models to account for flux outside the measurement aperture, were applied to both the measured fluxes and their uncertainties.

The resulting photometry (in nanojanskys) is presented in Table 1 and the SED is shown in Figure 2. Our measurements are consistent with previous measurements by J. Richard et al. (2011). Its red colors, already identified in the Spitzer/IRAC 3.6 and 4.5 μm bands, had previously been interpreted as evidence of a

ID	RA [deg]	DEC [deg]	F090W	F115W	F150W	F200W	F210M	F277W	F356W	F410M	F444W
S1	42.01369	-3.52636	321±23	444±29	427±33	520±32	458±33	627±73	1986±49	1109±43	2329±41
S2	42.01924	-3.53292	252±18	327±26	280±27	330±29	299±27	401±32	1328±32	685±25	1450±27

Table 1. Aperture fluxes (in nJy) for S1 and S2 across all JWST filters. Coordinates correspond to the F444W centroid positions of each image.

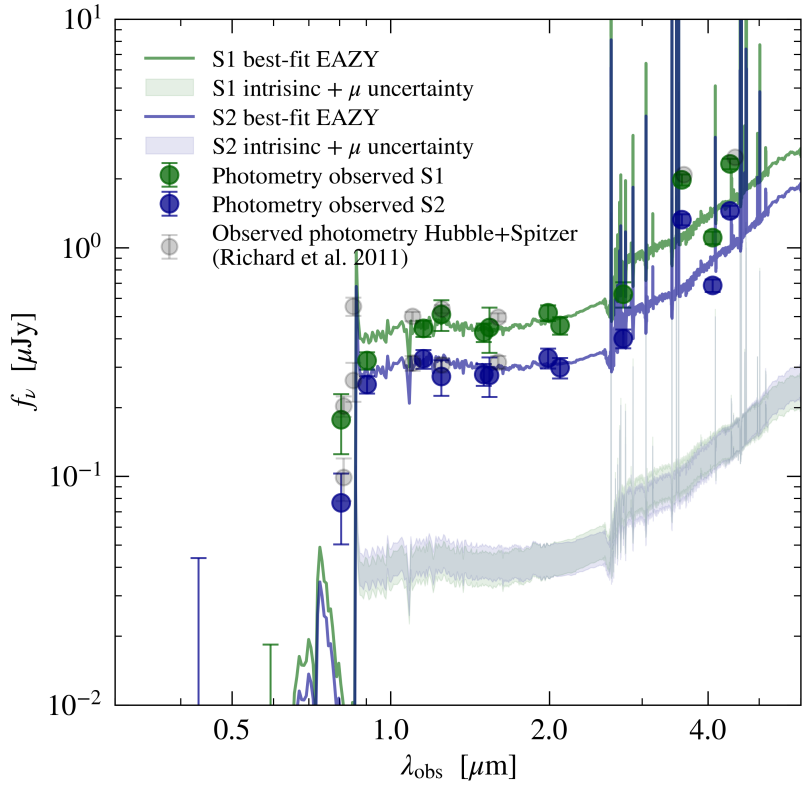

Figure 2. Spectral energy distribution (SED) derived from our aperture photometry for S1 (green points) and S2 (blue points). The solid lines show the best-fitting model to the total SED obtained with `EAZY`. The SED exhibits the characteristic "double-break" or "V-shape", corresponding to the Lyman and Balmer breaks, and its UV to optical colors are typical of the LRD population. Adopting the reported magnifications of $\mu_1 = 11.4 \pm 1.9$ and $\mu_2 = 7.3 \pm 1.2$ by J. Richard et al. (2011), we compute the intrinsic SED, with the uncertainties in μ represented by the shaded regions. The observed flux ratios (S1/S2) are in perfect agreement with the predicted μ_1/μ_2.

strong Balmer break and thus a massive galaxy with an old stellar population (J. Richard et al. 2011). Our new JWST/NIRCam photometry confirms that the discontinuity indeed falls at the Balmer break, producing the characteristic "double-break" (or "V-shape" when plotted in f_λ) SED. The observed colors (for both S1 and S2) are:

$$(\mathrm{F150W} - \mathrm{F200W}) = 0.2$$
$$(\mathrm{F277W} - \mathrm{F356W}) = 1.3$$
$$(\mathrm{F277W} - \mathrm{F444W}) = 1.4.$$

These colors match the photometric selection criteria now used for selecting LRDs in the literature (J. E. Greene et al. 2024; D. D. Kocevski et al. 2024).

This LRD is exceptionally bright, ranking among the brightest known on the sky. The observed fluxes are comparable to the ultra-luminous LRD reported by I. Labbe et al. (2024) and nearly two magnitudes brighter than the only other strongly lensed case known to date (L. J. Furtak et al. 2023, 2024).

Fitting the total observed photometry with `EAZY` (G. B. Brammer et al. 2008) (assuming a standard FSPS-based template set; tweak_fsps_QSF_12_v3) yields the solid model curves shown in Figure 2, which reproduce the measured fluxes well. The high fluxes in the F356W and F444W bands are interpreted as strong emission lines (e.g., Hβ + [OIII] and Hα), falling within these filters at this redshift. To illustrate the intrinsic SED, we scale the best-fitting model by the magnifica-

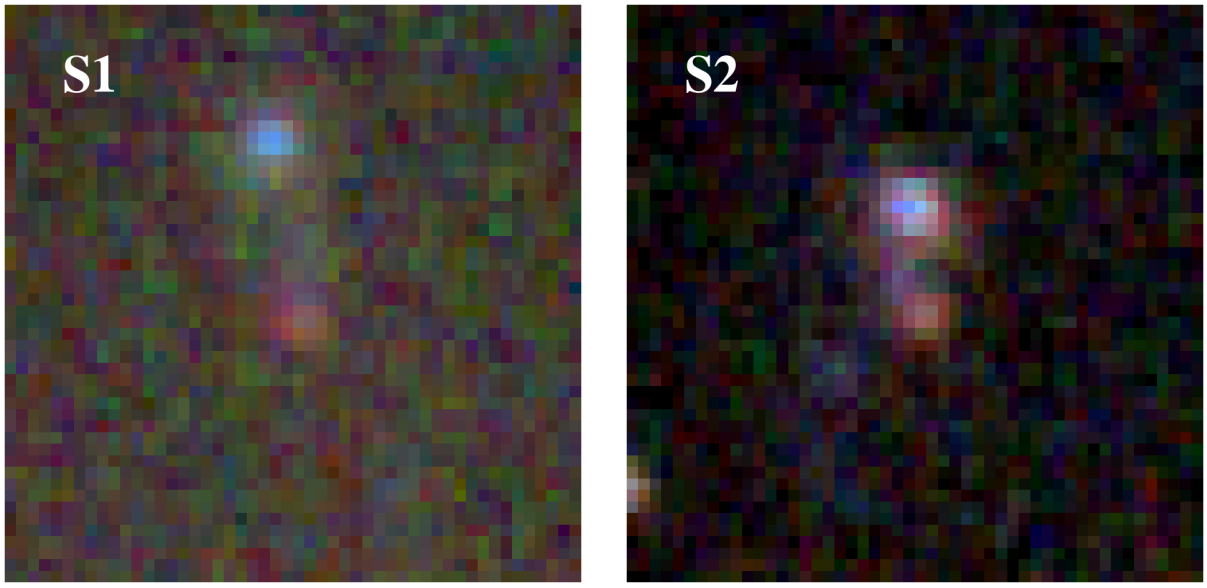

Figure 3. RGB image stamps constructed using filters F200W, F150W, and F115W for the two lensed images: S1 (left) and S2 (right). Both images are $1'' \times 1''$. In this work, we focus on image S2, as it lies in a relatively dark region of the sky with minimal contamination from intracluster light (ICL), whereas S1 is embedded in a brighter ICL background. We identify a prominent blue component, red component, and a connecting bridge-like structure, and model their surface brightness profiles as described in the text.

tions derived by J. Richard et al. (2011), with the corresponding uncertainties in μ represented by the shaded regions. We perform this for both S1 and S2 individually. Within the uncertainties, the two demagnified SEDs lie essentially on top of each other, lending confidence to the adopted magnification ratios. The intrinsic best-fit model yields a stellar mass of $M_\star \approx 6 \times 10^9 \mathrm{M}_\odot$, fully consistent with the conclusions of J. Richard et al. (2011).

The interpretation of an old stellar population proposed more than a decade ago, before LRDs were recognized as a distinct class, now sits at the center of current debates about the origin of LRD emission. In Section 4 we return to this and re-evaluate the SED using the full leverage of the new JWST data.

3. COMPONENT DECOMPOSITION

3.1. *Visual Morphology*

The morphology of the lensed galaxy, seen in both images S1 and S2, is complex and reveals multiple distinct components, as highlighted in Figure 3. The system clearly consists of two bright spatially distinct components: a compact region that dominates in the rest-frame UV and a component that becomes prominent at longer wavelengths. We further identify a fainter "bridge" structure that connects these two components.

3.2. *Sérsic Profile Fitting*

We perform surface brightness profile fitting using GALFIT (C. Y. Peng et al. 2002, 2010) with J. L. Sersic (1968) profiles across all available bands to quantify the morphology. The analysis focuses on image S2, as it lies in a relatively dark region of the sky with minimal contamination from intracluster light (ICL), whereas S1 is embedded in a brighter ICL background, making it less suitable for reliable profile fitting. The free parameters include galaxy position (x, y), effective radius along the major axis (r_e), Sérsic index (n), integrated magnitude (Mag), axis ratio (b/a), and position angle (PA). Prior to fitting, we identify and mask contaminating sources using sigma-clipped statistics with a 5-pixel filter size to estimate the background and RMS (σ). After background subtraction, images are convolved with a 2D Gaussian kernel (FWHM = 3 pixels), and sources above 1σ are masked. The mask is then refined to preserve both components of the target source while excluding nearby contaminants. We let r_e vary between 0.5-50 pixels, b/a between 0.1-1, and the magnitude between 1 and 100 mag. Radii are circularized with $r_\mathrm{e,circ} = \sqrt{b/a}\, r_\mathrm{e}$. As a first step, we fit the F200W image, which provides the highest S/N at optimal resolution, in order to determine accurate initial centroid positions for all components. These F200W-derived positions are then used as initial guesses in the fits to the other bands, and we allow the centroids in both x and y to vary only within

$\pm 0.04''$, corresponding to ± 2 pixels in the SW images and ± 1 pixel in the LW images.

We first attempt two-component fits (see Appendix A), which generally produce good residuals and capture the overall morphology well. However, in the short-wavelength (SW) bands, the red component appears artificially large because the model partially attributes the flux from the extended bridge-like emission to it. The bridge has a distinct color (see Figure 3), suggesting a physically different origin of emission. Motivated by this, we also test three-component models, which significantly improve the residuals in these bands (see Figure 4). In the long-wavelength (LW) bands, the bridge component becomes too faint and is likely blended with the blue and red components. As a result, GALFIT assigns its magnitude to the upper limit (Mag = 100), thus effectively removing it from the model.

Across both fitting approaches, the blue component is the most stable and well-constrained. Initial fits give $n \sim 1$–2, depending on how the bridge emission is treated and the effective radius of the blue component remains robust whether n is fixed or left free. We choose to adopt $n = 1.5$ (fixed) for all components while allowing the remaining parameters to vary freely.

We estimate uncertainties on the best-fit parameters (magnitude, r_e, and b/a) using injection–recovery simulations. The best-fit model for each component is inserted into 100 randomly selected empty-sky regions and convolved with either an empirical PSF or WebbPSF. For each parameter, we report the best-fit value measured in the real image, while the uncertainties correspond to the 16th–84th percentile range of the recovered distributions, computed relative to the simulation median. This procedure captures the impact of sky background variations, and PSF variations, but does not account for systematic uncertainties associated with different plausible models (e.g., two- vs. three-component fits), which in some bands may exceed the quoted errors.

3.3. *Wavelength-Dependent Structural Parameters*

The structural parameters derived from our modeling across all bands are presented in Table 2. These values are reported in the observed frame and do not yet account for gravitational lensing. In Section 5, we reconstruct the intrinsic (source-plane) morphology. The central values in the table correspond to the best-fit model parameters derived from the real image in each band. The associated uncertainties are obtained from simulations and reflect the 16th–84th percentile range of the recovered distributions.

Figure 4 shows the fitting results corresponding to the best-fit model parameters listed in the table. For each filter (rows), the figure displays the observed image (left), mask with pixels that are ignored during fitting (second column), the best-fitting model (third column), and the residual image (right). The GALFIT models match the data closely, with minimal residuals and a consistent separation between the blue and red components of $d_{\rm sep} \sim 0.18''$ in S2. While we do not perform full profile fitting for the other lensed image (S1), we do model the centroid positions of the blue and red component, and find a robust separation of $d_{\rm sep} \sim 0.3''$ across

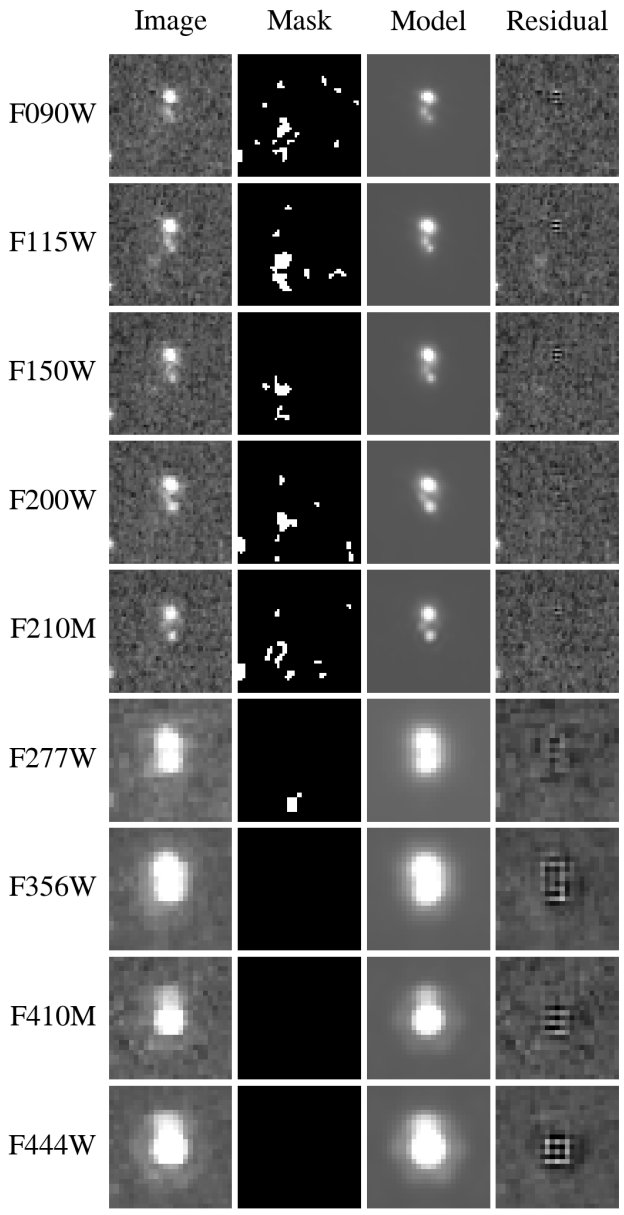

Figure 4. GALFIT best-fit models for S2. For each filter, we show (from left to right): the original image, fitting mask, best-fit model, and residual. The overall fits are good, with minimal residuals in most bands.

Band		Mag	b/a	r_e(pix)	$d_{sep}(''$)
F090W	Red	$28.6^{+0.6}_{-0.6}$	$0.9^{+0.1}_{-0.0}$	$1.4^{+2.4}_{-0.8}$	0.177
	Blue	$26.3^{+0.0}_{-0.1}$	$0.7^{+0.1}_{-0.0}$	$1.1^{+0.1}_{-0.1}$	
	Bridge	$27.2^{+0.5}_{-0.5}$	$0.6^{+0.3}_{-0.2}$	$3.9^{+1.9}_{-0.8}$	
F115W	Red	$28.5^{+0.3}_{-0.4}$	$0.6^{+0.3}_{-0.1}$	$0.8^{+0.9}_{-0.3}$	0.183
	Blue	$25.9^{+0.1}_{-0.0}$	$0.8^{+0.0}_{-0.1}$	$1.5^{+0.3}_{-0.1}$	
	Bridge	$26.7^{+0.4}_{-0.2}$	$0.6^{+0.2}_{-0.1}$	$4.1^{+0.9}_{-1.1}$	
F150W	Red	$27.7^{+0.3}_{-0.4}$	$0.7^{+0.2}_{-0.1}$	$1.1^{+1.1}_{-0.6}$	0.186
	Blue	$25.9^{+0.1}_{-0.0}$	$0.7^{+0.0}_{-0.1}$	$1.7^{+0.3}_{-0.3}$	
	Bridge	$27.0^{+0.7}_{-0.7}$	$0.7^{+0.3}_{-0.4}$	$4.0^{+4.9}_{-1.5}$	
F200W	Red	$27.0^{+0.1}_{-0.1}$	$0.8^{+0.2}_{-0.2}$	$1.4^{+0.6}_{-0.6}$	0.176
	Blue	$25.8^{+0.1}_{-0.1}$	$0.6^{+0.1}_{-0.1}$	$2.1^{+0.6}_{-0.4}$	
	Bridge	$28.1^{+0.4}_{-0.7}$	$0.1^{+0.2}_{-0.0}$	$1.9^{+2.4}_{-1.4}$	
F210M	Red	$27.2^{+0.1}_{-0.1}$	$0.6^{+0.2}_{-0.1}$	$0.5^{+0.3}_{-0.0}$	0.177
	Blue	$25.9^{+0.1}_{-0.1}$	$0.8^{+0.1}_{-0.1}$	$1.9^{+0.3}_{-0.9}$	
	Bridge	$28.4^{+0.5}_{-0.7}$	$0.1^{+0.3}_{-0.0}$	$0.8^{+1.8}_{-0.3}$	
F277W	Red	$25.7^{+0.1}_{-0.9}$	$0.8^{+0.1}_{-0.1}$	$1.9^{+0.5}_{-0.3}$	0.175
	Blue	$25.4^{+0.2}_{-0.1}$	$0.9^{+0.1}_{-0.4}$	$1.8^{+0.4}_{-0.6}$	
F356W	Red	$24.5^{+0.1}_{-0.3}$	$0.7^{+0.1}_{-0.1}$	$1.5^{+0.1}_{-0.5}$	0.176
	Blue	$24.4^{+0.3}_{-0.1}$	$0.9^{+0.1}_{-0.7}$	$1.6^{+0.4}_{-0.5}$	
F410M	Red	$24.5^{+0.4}_{-0.0}$	$0.9^{+0.0}_{-0.1}$	$1.0^{+0.3}_{-0.1}$	0.188
	Blue	$26.6^{+0.7}_{-0.4}$	$0.8^{+0.2}_{-0.1}$	$0.9^{+0.8}_{-0.0}$	
F444W	Red	$23.7^{+0.0}_{-0.1}$	$0.9^{+0.0}_{-0.1}$	$1.2^{+0.1}_{-0.4}$	0.188
	Blue	$25.7^{+0.5}_{-0.2}$	$0.7^{+0.3}_{-0.2}$	$1.3^{+0.8}_{-0.0}$	

Table 2. Structural modeling results for S2 using GALFIT. We report the best-fit parameters corresponding to Figure 4. The uncertainties are derived from 100 simulations and represent the 16th and 84th percentiles of the recovered parameter distributions.

the bands. We revisit the comparison between the separations for S1 and S2 in Section 5.

The blue component is consistently compact but resolved, with effective radii of $\sim 0.02 - 0.04''$ in the SW bands and increasing to $\sim 0.04 - 0.08''$ at longer wavelengths. These sizes are well constrained across filters and show no strong dependence on modeling assumptions (see Appendix A).

The red component is only marginally resolved and more difficult to isolate due to its proximity to the bridge. In the short-wavelength filters, its inferred size depends sensitively on how the bridge is modeled, as the boundary between the two components is hard to define. This issue is discussed in more detail in Appendix A. The associated modeling uncertainties are incorporated into our simulations and are reflected in the broad error bars reported for the SW bands in Table 2.

Given the extreme compact appearance of the red component, a natural question arises: could it simply be a point source? To explore this possibility, we fit a PSF model across all bands. The PSF fits perform reasonably well in the medium-band filters, particularly in F210M, where the fitted size almost reaches the lower limit of 0.5 pixels, and in F410M, where it remains close to 1.0 pixel. This suggests that the red component is extremely compact and may be unresolved at these wavelengths. However, in the wide-band filters, especially F277W and F356W, the PSF models leave significant residuals (see Appendix B), confirming that the red component is genuinely resolved in these bands. These two filters also yield the largest measured sizes (0.06-0.08″), for both the red and blue component.

Taken together, the results reveal a structurally complex system composed of a red component, a blue component, and a connecting bridge. Their structural parameters vary with wavelength, hinting at different physical contributions to the emission in each band, such as compact stellar and/or AGN continuum, along with more extended nebular line emission.

3.4. *Evidence for Low Surface Brightness Emission*

The current model includes three distinct components: the blue, red, and bridge component. Beyond these, there is evidence for an additional, more extended structure. In the segmentation maps of the SW bands (see Figure 4), a consistently detected region appears in the southeast direction, with an extent of at least $\sim 0.3''$. A similar hint of extended flux is visible in the F277W and F356W images, and is also clearly evident in the residuals shown in Appendix B with an extent of $\sim 0.6''$. Notably, this feature is harder to detect in S1 due to the significantly higher background from the surrounding ICL, but it is present. Due to the higher magnification and the parity flip (see Section 5.1), it appears on the opposite side and at a larger apparent separation. This provides further confirmation that the emission is physically associated with this LRD.

Further evidence comes from the flux budget. In the rest-frame UV bands, the summed flux of the three modeled components is up to ∼25% lower than the flux measured through apertures. This deficit is naturally explained if a non-negligible fraction of the system's light resides in faint, low–surface-brightness emission that is present in the pixels but not included in the GALFIT models, which only fit the three brightest components.

Independent support for an extended structure comes from previous ground-based spectroscopic observations. DEIMOS spectroscopy reveals spatially extended Lyα emission for S2 (their image 5.2) with a diameter of $\sim 3''$ (corresponding to $\sim$ 5 kpc in the source plane) along the slit direction (J. Richard et al. 2011). Notably, the DEIMOS slit was aligned roughly along the same south-

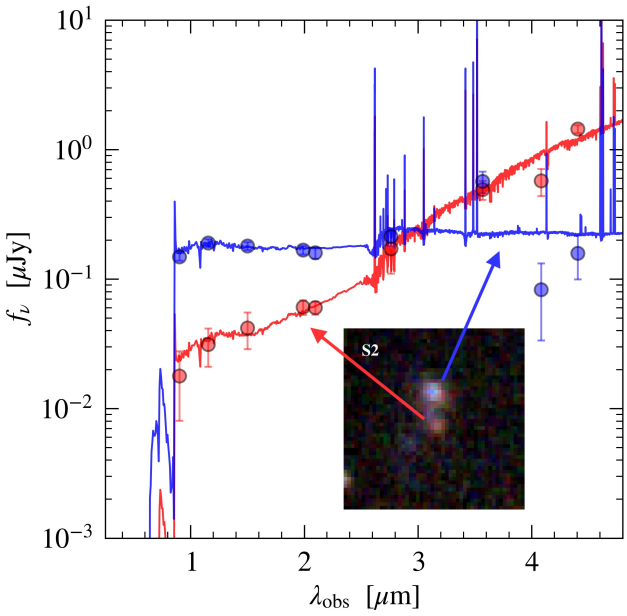

Figure 5. SED decomposition of the spatially resolved components derived from GALFIT modeling (red, blue), shown as colored points. Solid lines show best-fit EAZY fits, which assume simple stellar population templates. The red component has a steeply rising SED, while the blue component shows a relatively flat rest-frame UV continuum characteristic of young, unobscured star formation.

east direction as the extended feature identified in our JWST segmentation maps.

All of this suggests that the system hosts additional, low–surface-brightness emission beyond the three compact components modeled in our fits, though this extended structure is only weakly detected in the current JWST imaging. We return to this in Section 5, which presents the full source-plane reconstruction and the complete intrinsic morphology of the system.

4. SPECTRAL ENERGY DISTRIBUTION: SPLITTING AND FITTING

Having established the structural decomposition into separate components, we next determine their spectral properties, focusing specifically on the blue and red components. To measure the light from each component across all filters, we fix the Sérsic parameters of all components to their F200W values and allow only the total magnitude to vary. This differs from the full structural fitting described in Section 3.2, where all parameters were left free; here we instead perform forced photometry in the remaining bands. Flux uncertainties are taken from the GALFIT simulations described above, which provide the 16th–84th percentile range of the recovered magnitudes for each component in each band. These magnitudes and uncertainties are then converted to flux densities to construct the component SEDs.

Figure 5 shows the resulting SEDs, with individual flux measurements from the decomposed forced photometry shown as scatter points. To guide the interpretation of the underlying stellar populations, we fit these fluxes using `EAZY` (G. B. Brammer et al. 2008), with a standard FSPS-based template set (tweak_fsps_QSF_12_v3). These templates assume purely stellar emission and exclude any AGN contribution. The best-fit models, shown as (blue and red solid), are fit directly to the observed fluxes, but the physical parameters quoted below are derived from the intrinsic (de-lensed, assuming $\mu_2 = 7.3$) SEDs.

At short wavelengths, the emission is dominated by the blue component, which shows a nearly flat SED in f_ν. It exhibits an enhancement in F356W due to the Hβ+[OIII] complex, and remains relatively flat toward the red. The blue component is well fit by a young, star-forming stellar population with low dust attenuation ($A_V \sim 0.07$), a stellar mass of $M_\star \sim 3 \times 10^8, \mathrm{M}_\odot$, and a star formation rate of SFR ~ 1 M$_\odot$ yr^{-1}. In contrast, the red component becomes increasingly dominant toward longer wavelengths with an extremely steep SED, overtaking the blue around the Balmer break. The best-fit model suggests a significantly older, more massive, and more dust-attenuated population, with $A_V \sim 2.6$ $M_\star \sim 6 \times 10^{10}\mathrm{M}_\odot$, and SFR ~ 10 M$_\odot$ yr^{-1}.

These component-based SED fits are consistent with previous results based on the ground-based spectra, which rely on the total integrated light. J. Richard et al. (2011) and D. P. Stark et al. (2015) inferred a two-component star-formation history, with a young, unobscured population and a much older and dustier component. Their derived star-formation rates from the Lyα luminosity ($\sim 2\,\mathrm{M}_\odot$ yr^{-1}) are likewise in line with the properties we find for the blue component.

However, the extremely red SED may also point to a non-stellar origin such as a reddened AGN (e.g. K. Inayoshi & R. Maiolino 2025; A. de Graaff et al. 2025; X. Ji et al. 2025). It is intriguing that this component begins to dominate exactly at the Balmer break, the same wavelength at which the characteristic inflection appears in LRD SEDs (D. J. Setton et al. 2024). If the emission is a stars+AGN composite, it is not obvious why the AGN would begin to dominate precisely at this point, though this recurring coincidence across LRDs may hint at a more fundamental connection.

Fully disentangling these components and determining the origin of their emission will require spatially resolved spectroscopy. As discussed in Section 3.3, there is some degeneracy between the red component and the

bridge in the three-component fits, such that small modeling shifts can alter the flux assigned to each, similar to the uncertainties in their sizes. The SEDs shown here should therefore be taken as indicative rather than definitive. Nevertheless, the relative SED shapes already prove to be highly informative. The blue component remains remarkably stable across the modeling (two vs three-comp fits; see Appendix A), demonstrating that its inferred SED shape is robust and largely insensitive to assumptions about the decomposition. Most importantly, the SED decomposition makes it unambiguous that the iconic "double-break" or "V-shaped" SED (in f_λ) of this LRD is not an intrinsic feature of a single component. Instead, it arises from the combined light of two physically distinct sources.

5. SOURCE-PLANE RECONSTRUCTION

5.1. *Lens Model*

We now turn to the intrinsic, delensed properties of the LRD. For this analysis, we use the publicly available Abell 383 lensing models released through the CLASH program (A. Zitrin et al. 2015)[4]. We adopt the average magnification from the two parametric reconstructions provided; `Lenstool` (E. Jullo et al. 2007) and `GLEE` (S. H. Suyu & A. Halkola 2010). The lens models provide maps of total magnification ($\mu_{\rm tot}$), convergence (κ), shear (γ) and deflections fields ($\alpha_{\rm x}, \alpha_{\rm y}$), computed at a source redshift of $z = 2.55$. Since our source is at $z = 6.027$ rather than the model redshift of $z = 2.55$, we apply a redshift-dependent scaling to the deflection, shear, and convergence maps, given by the ratio of angular diameter distances:

$$\beta = \frac{d_{\rm A}(z_{\rm lens}, z_{\rm s})/d_{\rm A}(0, z_{\rm s})}{d_{\rm A}(z_{\rm lens}, z_{\rm model})/d_{\rm A}(0, z_{\rm model})}. \quad (1)$$

Here $d_{\rm A}$ is the angular diameter distance between two redshifts, and with $z_{\rm lens} = 0.189$ (Abell 383), $z_{\rm model} = 2.55$ and our source at $z_{\rm s} = 6.027$, we find $\beta = 1.04$.

After applying this correction (e.g. $\kappa \to \beta\kappa$, $\gamma \to \beta\gamma$), we compute the tangential magnification as $\mu_{\rm tan} = 1/(1-\kappa-\gamma)$ and radial magnification as $\mu_{\rm rad} = 1/(1-\kappa+\gamma)$. The total magnification is given by the product $\mu_{\rm tot} = \mu_{\rm tan}\mu_{\rm rad} = 1/((1-\kappa)^2 - \gamma^2)$. Gravitational lensing magnifies the galaxy in both area and flux by $\mu_{\rm tot}$ while conserving surface brightness, such that $m_{\rm obs} = m_{\rm int} - 2.5\log(\mu_{\rm tot})$.

For S1, we find $\mu_{1,\rm tan} = -4.0$ (negative indicating parity flip), $\mu_{1,\rm rad} = 2.8$ and $|\mu_{1,\rm tot}| = 10.8$. For S2, we find $\mu_{2,\rm tan} = 4.3$, $\mu_{2,\rm rad} = 1.7$ and $\mu_{2,\rm tot} = 7.3$. The total magnification values are in agreement with the reported values by J. Richard et al. (2011). In addition, the predicted magnification ratio $\mu_{1,\rm tot}/\mu_{2,\rm tot}$ is also consistent with the observed S1/S2 flux ratio, which is stable across all bands at ∼1.4–1.6, providing confidence in the overall normalization of the model magnifications. We note, however, that substantial variations exist among different lens modeling methods, both in the total magnification as well as the decomposition into radial and tangential components. Typical uncertainties in cluster-core magnifications are of order ∼ 20% (A. Zitrin et al. 2015), representing an additional systematic uncertainty on all intrinsic quantities reported here.

[4] https://archive.stsci.edu/missions/hlsp/clash/a383/models/

5.2. *Direct Ray-tracing of the JWST Pixels*

To visualize the morphology implied by the lens model with minimal assumptions, we perform a direct, pixel–based ray-tracing reconstruction of the JWST images. For each detector pixel we compute the source-plane coordinate via $\beta(\theta) = \theta - \alpha(\theta)$ and trace its four pixel corners using the deflection maps (α_x, α_y). This maps every image-plane pixel to an irregular quadrilateral in the source plane. The procedure removes only the geometric distortions introduced by lensing while conserving surface brightness and retaining the effects of the JWST PSF and pixel sampling.

Figure 6 (left panel) shows the resulting warped-pixel reconstruction for a rest-frame UV image (F200W/F150W/F115W), analogous to Figure 3, and a rest-frame optical image (F444W/F356W/F277W). These examples uses the `Lenstool` model, and we confirm that the `GLEE` model yields qualitatively consistent results. In the UV warped-pixel reconstruction, the two dominant components remain clearly detected and offset from one another, consistent with the image plane. In the optical combination, the redder emission becomes more prominent. The strong green channel (F356W) likely reflects bright [O III]+Hβ emission coming from the blue component. When the PSF is delensed, it becomes anisotropically stretched, causing any compact source to appear elongated in the warped maps. These elongations are therefore not intrinsic, and the warped reconstructions are used only qualitatively. The intrinsic morphology is instead derived by fitting the components in the observed plane with PSF-corrected GALFIT models and then applying the magnification corrections, as we will show in the next section.

5.3. *Intrinsic Sizes and Separations from Magnification Corrections*

We now apply magnification corrections to the observed sizes and separations derived from the best-fit

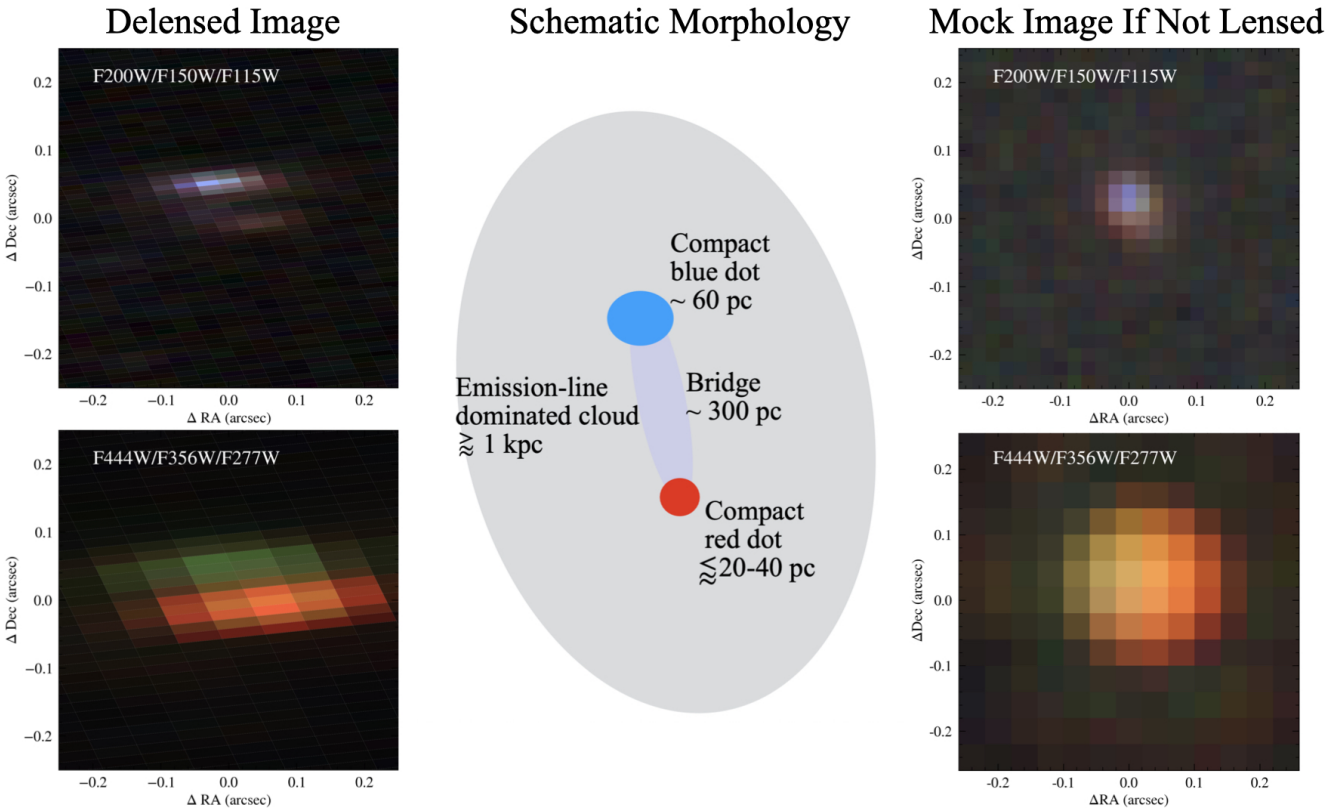

Figure 6. Left: Delensed warped-pixel reconstruction of the observed RGB images (F200W/F150W/F115W, top; F444W/F356W/F277W, bottom). Each pixel is mapped back to the source plane via the lens equation. Middle: Schematic reconstruction of the intrinsic morphology inferred from multi-band GALFIT modeling combined with lensing corrections. Right: Mock RGB images (F200W/F150W/F115W, top; F444W/F356W/F277W, bottom) in the absence of lensing. The best-fit models for each filter are corrected for lensing (see text), convolved with the regular JWST PSF and realistic background is added. These images demonstrate that, in the absence of magnification, all substructure would be compressed to scales comparable to the native JWST pixel size, making the intrinsic morphology challenging to uncover.

GALFIT models (Section 3.3). These are then converted into physical scales assuming a scale of $1'' = 5.8$ kpc at the source redshift of $z = 6.027$.

To compute the intrinsic separation between the red and blue components, we account for directional magnification along the measurement axis. The observed separation is corrected using $\mu_\theta = \sqrt{(\mu_{\rm tan}\cos(\theta))^2 + (\mu_{\rm rad}\sin(\theta))^2}$, where θ is the angle between the component separation vector and the local tangential direction. This gives a directional magnification μ_θ between $\mu_{\rm tan}$ (purely tangential, $\theta = 0°$) and $\mu_{\rm rad}$ (purely radial, $\theta = 90°$). The intrinsic separation is then given by $d_{\rm int} = d_{\rm obs}/\mu_\theta$. We estimate θ by determining the local shear orientation from the deflection maps. At the position of the red component in S2, we find $\theta = 33°$, resulting in $\mu_\theta = 3.7$. For S1, we find $\theta = 73°$, corresponding to $\mu_\theta = 2.9$.

Applying these corrections, we find an intrinsic separation of $\sim$0.05–0.06$''$ for S2, or about $\lesssim$3 SW pixels. For S1, the inferred separation is twice as large. Because S1 lies very close to the critical curve, its local magnification is likely less reliable than for S2. Moreover, Abell 383 is known to produce prominent radial arcs (D. J. Sand et al. 2005, 2008), and S1 falls in a region where radial stretching may be significant and potentially underestimated. We therefore adopt the S2 measurements as the more reliable estimate of the intrinsic separation. Further, the scale of $\sim$300 pc is identical to total half-light radius previously reported by J. Richard et al. (2011) using HST imaging.

For the intrinsic sizes of the blue and red component, the position angles are poorly constrained due to their compact and nearly circular morphologies. We therefore adopt an isotropic magnification correction, dividing the observed sizes by $\sqrt{\mu_{\rm tot}}$.

After correction, both components are found to be physically extremely compact. In the rest-UV (F150W, $\lambda_{\rm rest} \sim 200$ nm), the blue component has a typical size of $r_{\rm e,circ} \sim 60$ pc, and the red component $r_{\rm e,circ} \sim 40$ pc. Even tighter constraints are obtained from the medium-band filter F210M, yielding $r_{\rm e,circ} \lesssim 20$ pc for the red component. We interpret this as the most direct probe

of the intrinsic compactness of the red component, since the narrower bandwidth reduces contamination from potential strong emission lines.

In contrast, the emission appears significantly more extended in certain filters. In F277W, both components are resolved with $r_{\rm e,circ}$ ∼150 pc, implying a combined scale of ∼300 pc—comparable to the extent of the faint bridge-like structure connecting the two dots. This band traces the Balmer break and may therefore reflect a more spatially extended, older stellar population, but could also include contributions from [OII] emission, such as seen in other LRDs (e.g., M. Killi et al. 2024). In F356W, the emission is even more extended, reaching ∼0.6″ (∼1 kpc in the source plane). This scale matches the diffuse structures seen at short wavelengths (Section 3.4, which were masked during our GALFIT modeling) and agrees with earlier spectroscopic evidence for extended Lyα emission.

A schematic representation of the inferred source-plane morphology is shown in Figure 6 (middle panel). The system consists of two ultra-compact dots, each only tens of parsecs in size, connected by a ∼300 pc bridge-like component and embedded within a more diffuse, line-emitting cloud that extends to scales of up to ∼1 kpc. This interpretation is based on the available size constraints; the detailed spatial distribution of individual emission lines remains to be mapped with future spectroscopy.

6. DISCUSSION

The central result of this paper is the discovery of a newly identified Little Red Dot (LRD) that is doubly lensed by the galaxy cluster Abell 383. The two images, S1 and S2, are predicted to have total magnifications of $\mu \sim 11$ and $\mu \sim 7$, respectively, making this source the most highly magnified LRDs known.

Thanks to this extreme magnification, the system does not appear as a single "little red dot" but instead breaks into two compact components: a red dot and a spatially offset blue dot, separated by only ∼ 300 pc in the source plane. Both components are extraordinarily small. In the rest-UV their effective radii are only a few tens of parsecs, similar to the upper limit constraints of ∼35 pc L. J. Furtak et al. (2023), and comparable to sizes of high-redshift star clusters and clumps (e.g., E. Vanzella et al. 2023; A. Claeyssens et al. 2023).

Turning to the origin of the emission, the physical nature of these components remains under investigation. The blue component likely corresponds to a compact, star cluster. This is supported by its consistent morphology across all UV bands and a flat SED, indicative of continuum-dominated emission from a young stellar population.

The red component, on the other hand, is more enigmatic. One interpretation, motivated by its extreme compactness, is that it may host an accreting black hole. This scenario could be tested directly via high-resolution spectroscopy capable of resolving Keplerian rotation, as recently demonstrated in I. Juodžbalis et al. (2025).

Alternatively, the emission may be dominated by an evolved stellar population. The presence of a Balmer break in the SED suggests that the F277W morphology (with an effective radius of ∼ 150 pc) may trace the older stellar component. The best-fit stellar mass of $\sim 6 \times 10^{10}\ M_\odot$ within an effective radius would imply high stellar densities ($\Sigma_{\rm eff} \sim 4 \times 10^5 {\rm M}_\odot/{\rm pc}^2$) and therefore require substantial dynamical support. Using the scaling arguments of J. F. W. Baggen et al. (2024), such a system would be expected to exhibit velocity dispersions of order ∼ 700 km s^{-1}, corresponding to FWHM line widths of ∼ 1600 km s^{-1} and resolvable across ∼150 pc scale. However, if the stellar mass is enclosed within a smaller radius, as suggested by the more compact sizes in redder filters, the required velocity dispersions would be even higher.

A third possibility is that the optical emission arises from a composite system, consisting of a massive stellar cluster hosting an actively accreting black hole. Such a configuration is not only plausible but is in fact predicted by recent theoretical models, in which dense stellar systems assemble efficiently in a feedback-suppressed regime and then provide favorable conditions for early black hole growth (A. Dekel et al. 2023, 2025; F. Pacucci et al. 2025).[5] The morphology observed here, with its multi-component structure and, in particular, the size and stellar mass of the blue component, is in striking agreement with the characteristic properties predicted by these models.

Altogether, these results motivate a straightforward observational question: *what would this system look like in the absence of strong lensing?* Figure 6 (right panel) illustrates this. Here we take the best-fit intrinsic model by applying the appropriate magnification corrections to observed sizes and fluxes. We map the result onto a regular grid, convolve it with the JWST PSF, and add realistic background noise. We then generate an RGB composite using the F200W/F150W/F115W and F444W/F356W/F277W filter combinations. In the rest-UV composite (top panel) the red component, already faint in the rest-UV in the models, and further sup-

[5] We express our deepest condolences to the family and friends of Avishai Dekel.

pressed after demagnification, becomes effectively invisible, leaving the apparent structure dominated by the blue UV clump and bridge component. In the longer-wavelength composite (bottom panel) the system reduces to a single, PSF-like blob. In both cases, the morphology collapses into a nearly point-like, blended source, such that separating the red and blue components would be extremely difficult, if not impossible.

This has important implications for the broader LRD population. Features that we can spatially resolve here would normally be blended together. The most important example is the characteristic V-shaped SED. In this system, the V-shape is spatially resolved: our component-based SED decomposition shows that it is simply the superposition of the blue and red components. The same holds for the fluxes in F277W and F356W, filters that may trace the Balmer break and emission-line complexes such as [OII] and [OIII]+Hβ, respectively, where both components contribute comparable flux and are individually resolved. As a result, emission-line properties commonly attributed to a single compact region in LRDs need not originate from a single physical component. Instead, we might even expect the observed spectra to reflect a mixture of line widths, equivalent widths, and apparent Balmer-break signatures arising from physically distinct regions, rather than requiring one region to simultaneously reproduce all characteristic features.

Looking ahead, this system provides an important benchmark for interpreting LRDs more generally. Improved lens modeling for Abell 383, by incorporating the new JWST imaging will further refine the magnification field and hence the intrinsic sizes and separations. High-resolution spectroscopy, ideally with JWST/NIRSpec IFU, will be crucial for disentangling the stellar and non-stellar contributions to the emission, mapping their kinematics, and linking the spatially resolved structure to the integrated emission-line diagnostics used for unlensed LRDs. More broadly, the discovery of additional strongly lensed LRDs with resolved internal structure will be essential to determine whether the configuration seen here is a rare phenomenon or a common configuration of Little Red Dots.

ACKNOWLEDGMENTS

This work used the following python packages: `Matplotlib` (J. D. Hunter 2007), `SciPy` (P. Virtanen et al. 2020), `NumPy` (S. van der Walt et al. 2011), `AstroPy` (Astropy Collaboration et al. 2022) and `colossus` (B. Diemer 2018) and `photutils` (L. Bradley et al. 2025).

APPENDIX

A. GALFIT MODELING WITH TWO COMPONENTS

Figure 7 and Table 3 show the two–component GALFIT fits. While the overall fits are reasonable, the red component often appears artificially extended due to contamination from the bridge-like emission. This likely overestimates its size because the bridge and red component have very distinct colors (see Figure 3). This motivates the use of three-component models in these bands used in the main text. However, even with three components, some degeneracy remains in how flux is distributed between the red component and the bridge. When the bridge is modeled as brighter or more extended, the fitted size of the red component becomes smaller, and vice versa. Fortunately, the recovery simulations capture these effects well: in some cases, most of the emission is assigned to the bridge, making the red component very compact; in others, the red component absorbs more of the overlapping flux. This variation leads to the broad size uncertainties quoted in Table 2. The blue component is largely unaffected by this degeneracy, with best-fit structural parameters that remain consistent with those reported in Table 2.

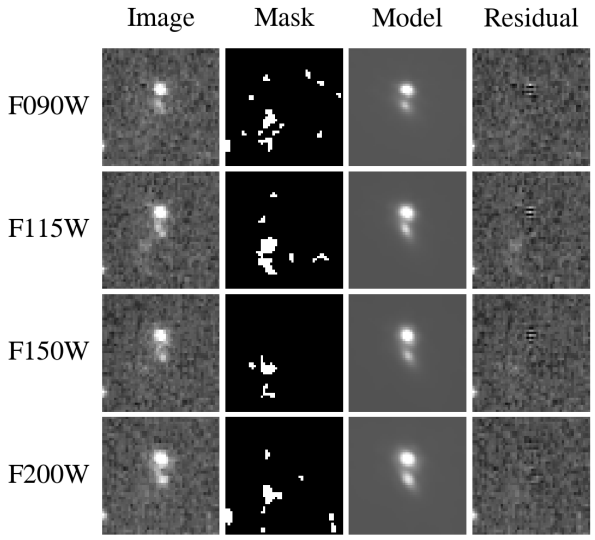

Figure 7. Two-component GALFIT modeling results for the short-wavelength (SW) bands (F090W, F115W, F150W, F200W). For each filter, we show (from left to right): the original image, fitting mask, best-fit model, and residual.

Band		Mag	r_e (pix)	b/a	Sep ($''$)
F090W	Red	27.0	3.8	0.6	0.13
	Blue	26.3	1.1	0.7	
F115W	Red	26.5	4.5	0.4	0.14
	Blue	25.9	1.5	0.8	
F150W	Red	26.6	4.3	0.4	0.17
	Blue	25.8	1.8	0.7	
F200W	Red	26.6	3.1	0.3	0.17
	Blue	25.8	2.1	0.7	

Table 3. GALFIT model parameters for S2 using two components (red, blue). Columns give integrated magnitude, effective radius (r_e, in pixels), axis ratio (b/a), and the separation between the red and blue components (in arcseconds), computed from the best-fit (x, y) GALFIT positions.

B. GALFIT MODELING WITH PSF TO RED COMPONENT

Figure 8 shows the PSF-only fits to the red component and residuals for the wide-band filters F277W and F356W. In both cases, significant residual structure remains, demonstrating that the red component is resolved in these bands.

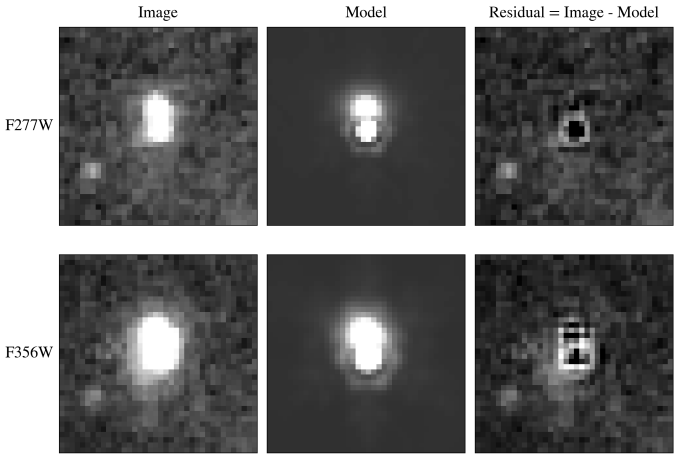

Figure 8. PSF-only fits to the red component for F277W and F356W. Left: observed cutouts. Middle: best-fit models where the red component is fit with only the PSF. Right: residual images (image-model), showing significant structure that demonstrates the red component is resolved in these bands.

REFERENCES

Akins, H. B., Casey, C. M., Allen, N., et al. 2023, ApJ, 956, 61, doi: 10.3847/1538-4357/acef21

Akins, H. B., Casey, C. M., Lambrides, E., et al. 2024, arXiv e-prints, arXiv:2406.10341, doi: 10.48550/arXiv.2406.10341

Akins, H. B., Casey, C. M., Berg, D. A., et al. 2025, ApJL, 980, L29, doi: 10.3847/2041-8213/adab76

Ananna, T. T., Bogdán, Á., Kovács, O. E., Natarajan, P., & Hickox, R. C. 2024, ApJL, 969, L18, doi: 10.3847/2041-8213/ad5669

Astropy Collaboration, Price-Whelan, A. M., Lim, P. L., et al. 2022, ApJ, 935, 167, doi: 10.3847/1538-4357/ac7c74

Baggen, J. F. W., van Dokkum, P., Labbé, I., et al. 2023, ApJL, 955, L12, doi: 10.3847/2041-8213/acf5ef

Baggen, J. F. W., van Dokkum, P., Brammer, G., et al. 2024, ApJL, 977, L13, doi: 10.3847/2041-8213/ad90b8

Barro, G., Pérez-González, P. G., Kocevski, D. D., et al. 2024, ApJ, 963, 128, doi: 10.3847/1538-4357/ad167e

Begelman, M. C., & Dexter, J. 2025, arXiv e-prints, arXiv:2507.09085, doi: 10.48550/arXiv.2507.09085

Begelman, M. C., Volonteri, M., & Rees, M. J. 2006, MNRAS, 370, 289, doi: 10.1111/j.1365-2966.2006.10467.x

Bradley, L., Sipőcz, B., Robitaille, T., et al. 2025, astropy/photutils: 2.2.0, 2.2.0 Zenodo, doi: 10.5281/zenodo.14889440

Brammer, G., Strait, V., Matharu, J., & Momcheva, I. 2022, grizli, 1.5.0 Zenodo, doi: 10.5281/zenodo.6672538

Brammer, G. B., van Dokkum, P. G., & Coppi, P. 2008, ApJ, 686, 1503, doi: 10.1086/591786

Burke, C. J., Stone, Z., Shen, Y., & Jiang, Y.-F. 2025, arXiv e-prints, arXiv:2511.16082, doi: 10.48550/arXiv.2511.16082

Carranza-Escudero, M., Conselice, C. J., Adams, N., et al. 2025, ApJL, 989, L50, doi: 10.3847/2041-8213/adf73d

Chen, C.-H., Ho, L. C., Li, R., & Inayoshi, K. 2025, ApJL, 989, L12, doi: 10.3847/2041-8213/adee0a

Claeyssens, A., Adamo, A., Richard, J., et al. 2023, MNRAS, 520, 2180, doi: 10.1093/mnras/stac3791

de Graaff, A., Rix, H.-W., Naidu, R. P., et al. 2025, arXiv e-prints, arXiv:2503.16600, doi: 10.48550/arXiv.2503.16600

Dekel, A., Sarkar, K. C., Birnboim, Y., Mandelker, N., & Li, Z. 2023, MNRAS, 523, 3201, doi: 10.1093/mnras/stad1557

Dekel, A., Dutta Chowdhury, D., Lapiner, S., et al. 2025, arXiv e-prints, arXiv:2511.07578, doi: 10.48550/arXiv.2511.07578

D'Eugenio, F., Nelson, E., Ji, X., et al. 2025a, arXiv e-prints, arXiv:2510.00101, doi: 10.48550/arXiv.2510.00101

D'Eugenio, F., Maiolino, R., Perna, M., et al. 2025b, arXiv e-prints, arXiv:2503.11752, doi: 10.48550/arXiv.2503.11752

Diemer, B. 2018, ApJS, 239, 35, doi: 10.3847/1538-4365/aaee8c

Furtak, L. J., Zitrin, A., Plat, A., et al. 2023, ApJ, 952, 142, doi: 10.3847/1538-4357/acdc9d

Furtak, L. J., Labbé, I., Zitrin, A., et al. 2024, Nature, 628, 57, doi: 10.1038/s41586-024-07184-8

Gloudemans, A. J., Duncan, K. J., Eilers, A.-C., et al. 2025, ApJ, 986, 130, doi: 10.3847/1538-4357/adddb9

Greene, J. E., Labbe, I., Goulding, A. D., et al. 2024, ApJ, 964, 39, doi: 10.3847/1538-4357/ad1e5f

Harikane, Y., Zhang, Y., Nakajima, K., et al. 2023, ApJ, 959, 39, doi: 10.3847/1538-4357/ad029e

Hunter, J. D. 2007, Computing in Science and Engineering, 9, 90, doi: 10.1109/MCSE.2007.55

Hviding, R. E., de Graaff, A., Miller, T. B., et al. 2025, arXiv e-prints, arXiv:2506.05459, doi: 10.48550/arXiv.2506.05459

Inayoshi, K., & Maiolino, R. 2025, ApJL, 980, L27, doi: 10.3847/2041-8213/adaebd

Ji, X., Maiolino, R., Übler, H., et al. 2025, MNRAS, doi: 10.1093/mnras/staf1867

Jullo, E., Kneib, J.-P., Limousin, M., et al. 2007, New Journal of Physics, 9, 447, doi: 10.1088/1367-2630/9/12/447

Juodžbalis, I., Maiolino, R., Baker, W. M., et al. 2024, arXiv e-prints, arXiv:2403.03872, doi: 10.48550/arXiv.2403.03872

Juodžbalis, I., Marconcini, C., D'Eugenio, F., et al. 2025, arXiv e-prints, arXiv:2508.21748, doi: 10.48550/arXiv.2508.21748

Killi, M., Watson, D., Brammer, G., et al. 2024, A&A, 691, A52, doi: 10.1051/0004-6361/202348857

Kocevski, D. D., Onoue, M., Inayoshi, K., et al. 2023, ApJL, 954, L4, doi: 10.3847/2041-8213/ace5a0

Kocevski, D. D., Finkelstein, S. L., Barro, G., et al. 2024, arXiv e-prints, arXiv:2404.03576, doi: 10.48550/arXiv.2404.03576

Kokorev, V., Chisholm, J., Endsley, R., et al. 2024, ApJ, 975, 178, doi: 10.3847/1538-4357/ad7d03

Labbé, I., van Dokkum, P., Nelson, E., et al. 2023, Nature, 616, 266, doi: 10.1038/s41586-023-05786-2

Labbe, I., Greene, J. E., Matthee, J., et al. 2024, arXiv e-prints, arXiv:2412.04557, doi: 10.48550/arXiv.2412.04557

Leung, G. C. K., Finkelstein, S. L., Pérez-González, P. G., et al. 2025, ApJ, 992, 26, doi: 10.3847/1538-4357/adfcce

Maiolino, R., Scholtz, J., Curtis-Lake, E., et al. 2024, A&A, 691, A145, doi: 10.1051/0004-6361/202347640

Matthee, J., Naidu, R. P., Brammer, G., et al. 2024, ApJ, 963, 129, doi: 10.3847/1538-4357/ad2345

Naidu, R. P., Matthee, J., Katz, H., et al. 2025, arXiv e-prints, arXiv:2503.16596, doi: 10.48550/arXiv.2503.16596

Pacucci, F., Hernquist, L., & Fujii, M. 2025, arXiv e-prints, arXiv:2509.02664, doi: 10.48550/arXiv.2509.02664

Peng, C. Y., Ho, L. C., Impey, C. D., & Rix, H.-W. 2002, AJ, 124, 266, doi: 10.1086/340952

Peng, C. Y., Ho, L. C., Impey, C. D., & Rix, H.-W. 2010, AJ, 139, 2097, doi: 10.1088/0004-6256/139/6/2097

Pérez-González, P. G., Barro, G., Rieke, G. H., et al. 2024, ApJ, 968, 4, doi: 10.3847/1538-4357/ad38bb

Planck Collaboration VI. 2020, A&A, 641, A6, doi: 10.1051/0004-6361/201833910

Postman, M., Coe, D., Benítez, N., et al. 2012, ApJS, 199, 25, doi: 10.1088/0067-0049/199/2/25

Richard, J., Kneib, J.-P., Ebeling, H., et al. 2011, MNRAS, 414, L31, doi: 10.1111/j.1745-3933.2011.01050.x

Rinaldi, P., Bonaventura, N., Rieke, G. H., et al. 2024, arXiv e-prints, arXiv:2411.14383, doi: 10.48550/arXiv.2411.14383

Sand, D. J., Treu, T., Ellis, R. S., & Smith, G. P. 2005, ApJ, 627, 32, doi: 10.1086/430298

Sand, D. J., Treu, T., Ellis, R. S., Smith, G. P., & Kneib, J.-P. 2008, ApJ, 674, 711, doi: 10.1086/524652

Santarelli, A. D., Farag, E., Bellinger, E. P., et al. 2025, arXiv e-prints, arXiv:2510.17952, doi: 10.48550/arXiv.2510.17952

Sersic, J. L. 1968, Atlas de Galaxias Australes

Setton, D. J., Greene, J. E., de Graaff, A., et al. 2024, arXiv e-prints, arXiv:2411.03424, doi: 10.48550/arXiv.2411.03424

Setton, D. J., Greene, J. E., Spilker, J. S., et al. 2025, ApJL, 991, L10, doi: 10.3847/2041-8213/ade78b

Stark, D. P., Richard, J., Charlot, S., et al. 2015, MNRAS, 450, 1846, doi: 10.1093/mnras/stv688

Suyu, S. H., & Halkola, A. 2010, A&A, 524, A94, doi: 10.1051/0004-6361/201015481

van der Walt, S., Colbert, S. C., & Varoquaux, G. 2011, Computing in Science and Engineering, 13, 22, doi: 10.1109/MCSE.2011.37

Vanzella, E., Claeyssens, A., Welch, B., et al. 2023, ApJ, 945, 53, doi: 10.3847/1538-4357/acb59a

Virtanen, P., Gommers, R., Oliphant, T. E., et al. 2020, Nature Methods, 17, 261, doi: 10.1038/s41592-019-0686-2

Wang, B., Leja, J., de Graaff, A., et al. 2024, ApJL, 969, L13, doi: 10.3847/2041-8213/ad55f7

Wang, B., Leja, J., Katz, H., et al. 2025, arXiv e-prints, arXiv:2508.18358, doi: 10.48550/arXiv.2508.18358

Weaver, J. R., Cutler, S. E., Pan, R., et al. 2024, ApJS, 270, 7, doi: 10.3847/1538-4365/ad07e0

Williams, C. C., Alberts, S., Ji, Z., et al. 2024, ApJ, 968, 34, doi: 10.3847/1538-4357/ad3f17

Zitrin, A., Fabris, A., Merten, J., et al. 2015, ApJ, 801, 44, doi: 10.1088/0004-637X/801/1/44